

Shadow Generation for Composite Image in Real-world Scenes

Yan Hong, Li Niu*, Jianfu Zhang, Liqing Zhang

MoE Key Lab of Artificial Intelligence, Shanghai Jiao Tong University

yanhong.sjtu@gmail.com, {ustcnewly, c.sis}@sjtu.edu.cn, zhang-lq@cs.sjtu.edu.cn

Abstract

Image composition targets at inserting a foreground object on a background image. Most previous image composition methods focus on adjusting the foreground to make it compatible with background while ignoring the shadow effect of foreground on the background. In this work, we focus on generating plausible shadow for the foreground object in the composite image. First, we contribute a real-world shadow generation dataset DESOBA by generating synthetic composite images based on paired real images and deshadowed images. Then, we propose a novel shadow generation network SGRNet, which consists of a shadow mask prediction stage and a shadow filling stage. In the shadow mask prediction stage, foreground and background information are thoroughly interacted to generate foreground shadow mask. In the shadow filling stage, shadow parameters are predicted to fill the shadow area. Extensive experiments on our DESOBA dataset and real composite images demonstrate the effectiveness of our proposed method.

1. Introduction

Image composition targets at copying a foreground object from one image and pasting it on another background image to produce a composite image. In recent years, image composition has drawn increasing attention from a wide range of applications in the fields of medical science, education, and entertainment [1, 46, 23]. Some deep learning methods [20, 3, 30, 2] have been developed to improve the realism of composite image in terms of color consistency, relative scaling, spatial layout, occlusion, and viewpoint transformation. However, the above methods mainly focus on adjusting the foreground while neglecting the effect of inserted foreground on the background such as shadow or reflection. In this paper, we focus on dealing with the shadow inconsistency between the foreground object and the background, that is, generating shadow for the foreground object according to background information, to

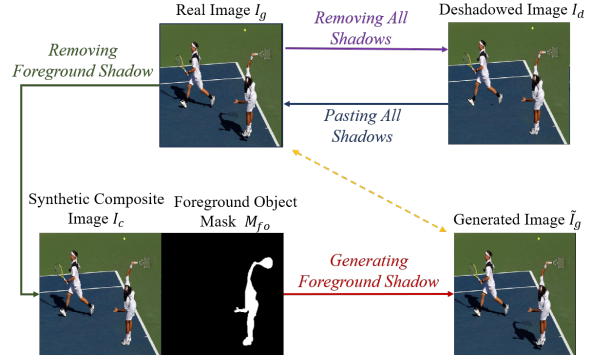


Figure 1. 1) The green arrows illustrate the process of acquiring paired data for training and evaluation. Given a ground-truth target image I_g , we manually remove all shadows to produce a deshadowed image I_d . Then, we randomly select a foreground object in I_g , and replace its shadow area with the counterpart in I_d to synthesize a composite image I_c without foreground shadow. I_c and I_g form a pair of input composite image and ground-truth target image. 2) The red arrow illustrates our shadow generation task. Given I_c and its foreground mask M_{fo} , we aim to generate the target image \tilde{I}_g with foreground shadow.

make the composite image more realistic.

To accomplish this image-to-image translation task, deep learning techniques generally require adequate paired training data, *i.e.*, a composite image without foreground shadow and a target image with foreground shadow. However, it is extremely difficult to obtain such paired data in the real world. Therefore, previous works [46, 23] insert a virtual object into 3D scene and generate shadow for this object using rendering techniques. In this way, a rendered dataset with paired data can be constructed, but it has two obvious drawbacks. First, the number of objects/scenes is very limited (*e.g.*, [23] only has 11 foreground objects) and the background scenes are very simple. Second, there exists large domain gap between rendered images and real-world images, which results in the inapplicability of rendered dataset to real-world image composition problem.

Considering the above drawbacks, we tend to build our own real-world shadow generation dataset by synthesizing

*Corresponding author.

composite image from a ground-truth target image with object-shadow pairs. We build our dataset on the basis of Shadow-Object Association (SOBA) dataset, which collects real-world images in complex scenes and provides annotated masks for object-shadow pairs. SOBA contains 3,623 pairs of shadow-object associations over 1000 photos. Based on SOBA dataset, we remove all the shadows to construct our DShadowed Shadow-Object Association (DESOBA) dataset, which can be used for shadow generation task. At the start, we tried to remove the shadows with the state-of-the-art deshadow methods [12, 17, 44, 18, 8]. However, their performance is far from satisfactory due to complex scenes. Thus, with shadow images and shadow masks from SOBA datasets, we employ professional photo editors to manually remove the shadows in each image to obtain deshadowed images. We require the background texture details to be preserved and the transition over shadow boundary to be smooth. One example of ground-truth target image \mathbf{I}_g and its deshadowed version \mathbf{I}_d is shown in Figure 1. To obtain paired training data for shadow generation task, we choose a foreground object with associated shadow in the ground-truth target image \mathbf{I}_g and replace its shadow area with the counterpart in the deshadowed image \mathbf{I}_d , yielding the synthetic composite image \mathbf{I}_c . In this way, pairs of synthetic composite image \mathbf{I}_c and ground-truth target image \mathbf{I}_g can be obtained.

With paired training data available, the shadow generation task can be defined as follows. Given an input composite image \mathbf{I}_c and the foreground object mask \mathbf{M}_{fo} , the goal is to generate realistic shadow for the foreground object, resulting in the target image $\tilde{\mathbf{I}}_g$ which should be close to the ground-truth \mathbf{I}_g (see Figure 1). For ease of description, we use foreground (*resp.*, background) shadow to indicate the shadow of foreground (*resp.*, background) object. Existing image-to-image translation methods [14, 48, 13, 21] can be used for shadow generation, but they cannot achieve plausible shadows without considering illumination condition or shadow property. ShadowGAN [46] was designed to generate shadows for virtual objects by combining a global discriminator and a local discriminator. ARShadowGAN [23] searched clues from background using attention mechanism to assist in shadow generation. However, the abovementioned methods failed to fully exploit background information and did not leverage typical illumination model, which motivates us to propose a novel Shadow Generation in the Real-world Network (SGRNet) to generate shadows for the foreground objects in complex scenes.

As illustrated in Figure 3, SGRNet consists of a shadow mask prediction stage and a shadow filling stage. In the shadow prediction stage, provided with a synthetic composite image \mathbf{I}_c and foreground object mask \mathbf{M}_{fo} , we design a foreground encoder to extract the required information of the foreground object and a background encoder to in-

fer illumination information from background. To achieve thorough foreground and background information interaction, a non-local attentional integration layer is employed to help generate shadow mask for the foreground object. The shadow filling stage is designed based on illumination model [17], which first predicts the shadow property and then edits the shadow area. Besides, we design a conditional discriminator to distinguish real object-shadow-image triplets from fake triplets, which can push the generator to produce realistic foreground shadow. To verify the effectiveness of our proposed SGRNet, we conduct comprehensive experiments on our DESOBA dataset and real composite images.

Our main contributions are summarized as follows: 1) we contribute the first real-world shadow generation dataset DESOBA using a novel data acquisition approach; 2) we design a novel two-stage network SGRNet to generate shadow for the foreground object in composite image; 3) extensive experiments demonstrate the effectiveness of our way to construct dataset and the superiority of our proposed network.

2. Related Work

2.1. Image Composition

Image composition targets at pasting a foreground object onto another background image to produce a composite image [20, 35, 37, 39, 23]. There are many issues that would significantly degrade the quality of composite images, such as unreasonable location of foreground or inconsistent color, illumination, geometry between foreground and background. Previous works attempted to solve one or some of the above issues. For example, image blending methods [26, 35, 45, 42] were developed to blend foreground and background more naturally. Image harmonization methods [47, 36, 29, 7, 6] were proposed to address the color and illumination discrepancy between foreground and background. Some other approaches [4, 34, 40] aimed to cope with the inconsistency of geometry, color, and boundary at the same time. However, the above methods did not consider the shadow effect of inserted foreground on background image, which is the focus of this paper.

2.2. Shadow Generation

Prior works on shadow generation can be divided into two groups: rendering based methods and image-to-image translation methods.

Shadow Generation via Rendering: This group of methods requires explicit knowledge of illumination, reflectance, material properties, and scene geometry to generate shadow for inserted virtual object using rendering techniques. However, such knowledge is usually unavailable in the real-world applications. Some methods [15, 16, 22] relied on

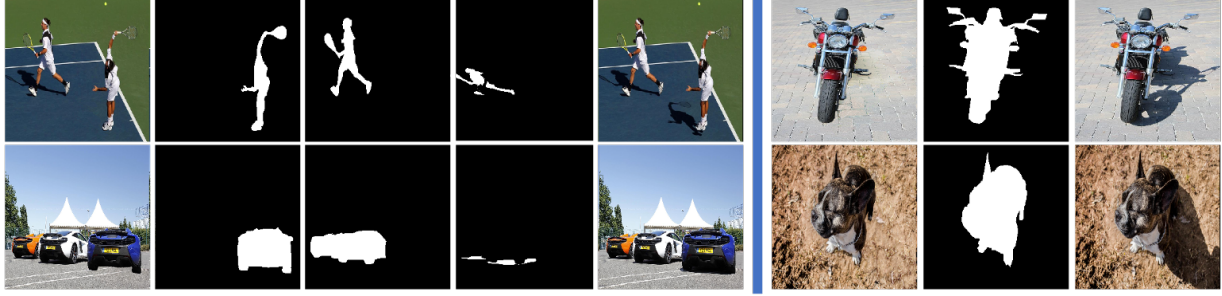


Figure 2. Some examples from our DESOBA dataset. BOS test image pairs with Background Object-Shadow (BOS) pairs are shown in the left subfigure, from left to right: synthetic composite image, foreground object mask, background object mask, background shadow mask, and ground-truth target image. BOS-free test image pairs are shown in the right subfigure, from left to right: synthetic composite image, foreground object mask, and ground-truth target image.

user interaction to acquire illumination condition and scene geometry, which is time-consuming and labor-intensive. Without user interaction, some methods [19, 9, 43, 1] attempted to recover explicit illumination condition and scene geometry based on a single image, but this estimation task is quite tough and inaccurate estimation may lead to terrible results [46].

Shadow Generation via Image-to-image Translation:

This group of methods learns a mapping from the input image without foreground shadow to the output with foreground shadow, without requiring explicit knowledge of illumination, reflectance, material properties, and scene geometry. Most methods within this group have encoder-decoder network structures. For example, the shadow removal method Mask-ShadowGAN [12] could be adapted to shadow generation, but the cyclic generation procedure failed to generate shadows in complex scenes. ShadowGAN [46] combined a global conditional discriminator and a local conditional discriminator to generate shadow for inserted 3D foreground objects without exploiting background illumination information. In [38], an adversarial image composition network was proposed for harmonization and shadow generation simultaneously, but it calls for extra indoor illumination dataset [10, 5]. ARShadowGAN [23] released Shadow-AR dataset and proposed an attention-guided network. Distinctive from the above works, our proposed SGRNet encourages thorough information interaction between foreground and background, and also leverages typical illumination model to guide network design.

3. Dataset Construction

We follow the training/test split in SOBA [32]. SOBA has 840 training images with totally 2,999 object-shadow pairs and 160 test images with totally 624 object-shadow pairs. For each image in the training set, to obtain more training image pairs, we use a subset of foreground objects with associated shadows each time. Specifically, given a

real image \mathbf{I}_g with n object-shadow pairs $\{(\mathbf{O}_i, \mathbf{S}_i) |_{i=1}^n\}$ and its deshadowed version \mathbf{I}_d without shadows $\{\mathbf{S}_i |_{i=1}^n\}$, we randomly select 1 or 2 foreground objects from \mathbf{I}_g and replace their shadow areas with the counterparts in \mathbf{I}_d , leading to a synthetic composite image \mathbf{I}_c . In this way, based on the training set of SOBA, we can obtain in total 11,316 training image pairs of synthetic composite images and ground-truth target images. In Section 4, for ease of description, we treat a subset of foreground objects as one whole foreground object.

For the test set, we only select 1 foreground object to obtain synthetic composite image each time. In this way, based on the test set of SOBA, we obtain 624 test image pairs. We divide test image pairs into two groups according to whether they have background object-shadow pairs, because they have different properties and need to be evaluated separately. Specifically, we refer to the test image pairs with Background Object-Shadow (BOS) pairs as BOS test image pairs, and the remaining ones as BOS-free test image pairs. Some examples of BOS test image pairs and BOS-free test image pairs are shown in Figure 2.

4. Our Method

Given a synthetic composite image \mathbf{I}_c without foreground shadow and the mask of foreground object \mathbf{M}_{fo} , our proposed Shadow Generation in the Real-world Network (SGRNet) targets at generating $\tilde{\mathbf{I}}_g$ with foreground shadow. Our SGRNet consists of two stages: a shadow mask prediction stage and a shadow filling stage (see Figure 3). In the shadow mask prediction stage, a shadow mask generator G_S with foreground branch and background branch is designed to generate shadow mask $\tilde{\mathbf{M}}_{fs}$. In the shadow filling stage, a shadow parameter predictor E_P and a shadow matte generator G_M are used to fill the shadow mask to produce the target image $\tilde{\mathbf{I}}_g$ with foreground shadow. Besides, a conditional discriminator D is used to enforce SGRNet to generate realistic shadow mask $\tilde{\mathbf{M}}_{fs}$ and target image $\tilde{\mathbf{I}}_g$.

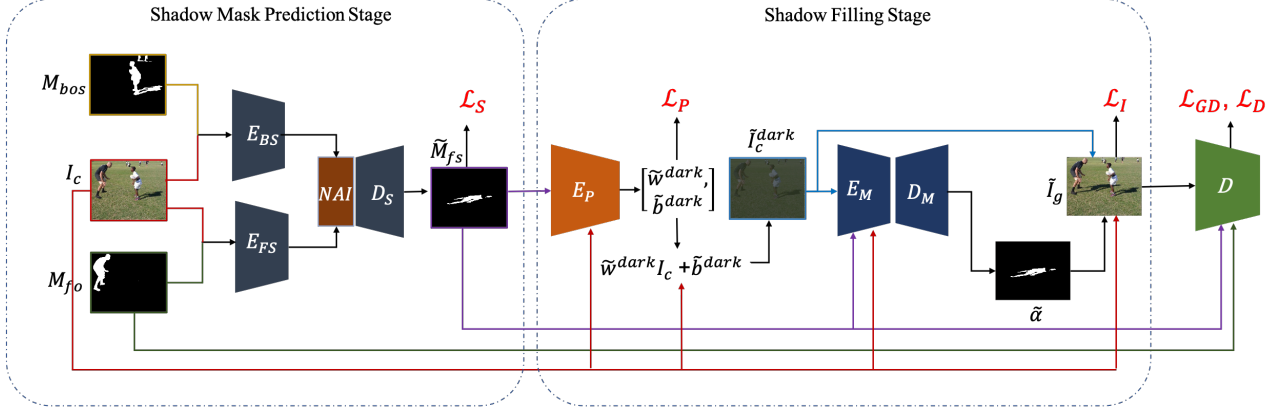


Figure 3. The framework of our SGRNet which consists of a shadow mask prediction stage and a shadow filling stage. In the shadow mask prediction stage, shadow mask \tilde{M}_{fs} is generated by the shadow mask generator composed of foreground encoder E_{FS} , background encoder E_{BS} , non-local attentional integration (NAI) layer, and decoder D_S . In the shadow filling stage, shadow parameters $\{\tilde{w}, \tilde{b}\}$ are predicted by E_P for producing darkened image \tilde{I}_c^{dark} , and shadow matte predictor $G_M = \{E_M, D_M\}$ generates shadow matte $\tilde{\alpha}$. The final target image \tilde{I}_g is obtained by blending \tilde{I}_c^{dark} and I_c using α .

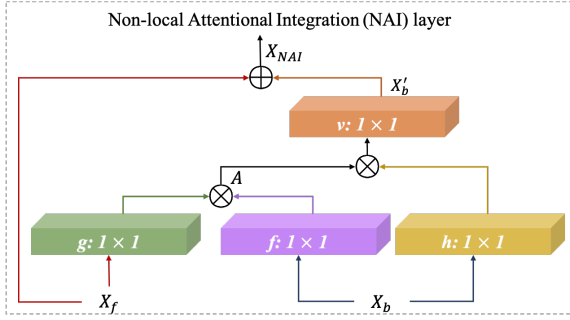


Figure 4. The architecture of our Non-local Attentional Integration (NAI) layer. X_f (*resp.*, X_b) is the foreground (*resp.*, background) feature and X_{NAI} is the output of NAI layer. g , f , h , and v are 1×1 convolutions. \otimes denotes matrix multiplication and \oplus denotes element-wise addition.

4.1. Shadow Mask Generator

The shadow mask generator G_S aims to predict the binary shadow mask \tilde{M}_{fs} of the foreground object. We adopt U-Net [27] structure consisting of an encoder E_S and a decoder D_S . To better extract foreground and background information, we split E_S into a foreground encoder E_{FS} and a background encoder E_{BS} . The foreground encoder E_{FS} takes the concatenation of input composite image I_c and foreground object mask M_{fo} as input, producing the foreground feature map $X_f = E_{FS}(I_c, M_{fo})$. The background encoder E_{BS} is expected to infer implicit illumination information from background. Considering that the background object-shadow pairs can provide important cues such as light direction, we use off-the-shelf LISA model [32] to predict background object-shadow

mask M_{bos} enclosing all background object-shadow pairs. The background encoder E_{BS} takes the concatenation of I_c and M_{bos} as input, producing the background feature map $X_b = E_{BS}(I_c, M_{bos})$.

The illumination information in different image regions may vary due to complicated scene geometry and light sources, which greatly increases the difficulty of shadow mask generation [46]. So it is crucial to attend relevant illumination information to generate foreground shadow. Inspired by previous attention-based methods [41, 33, 31], we use a Non-local Attentional Integration (NAI) layer shown in Figure 4 to help foreground feature map X_f attend relevant illumination information from background feature map X_b .

Firstly, $X_f \in \mathcal{R}^{H \times W \times C}$ and $X_b \in \mathcal{R}^{H \times W \times C}$ are projected to a common space by $f(\cdot)$ and $g(\cdot)$ respectively, where $f(\cdot)$ and $g(\cdot)$ are 1×1 convolutional layer with spectral normalization [24]. For ease of calculation, we reshape $f(X_b) \in \mathcal{R}^{W \times H \times \frac{C}{8}}$ (*resp.*, $g(X_f) \in \mathcal{R}^{W \times H \times \frac{C}{8}}$) into $\bar{f}(X_b) \in \mathcal{R}^{N \times \frac{C}{8}}$ (*resp.*, $\bar{g}(X_f) \in \mathcal{R}^{N \times \frac{C}{8}}$), in which $N = W \times H$. Then, we can calculate the affinity map between X_f and X_b :

$$A = \text{softmax}(\bar{g}(X_f)\bar{f}(X_b)^T). \quad (1)$$

With obtained affinity map A , we attend information from X_b and arrive at the attended feature map X'_b :

$$X'_b = v(A\bar{h}(X_b)), \quad (2)$$

where $\bar{h}(\cdot)$ means 1×1 convolutional layer followed by reshaping to $\mathcal{R}^{N \times \frac{C}{8}}$, similar to $\bar{f}(\cdot)$ and $\bar{g}(\cdot)$ in Eqn. 1. $v(\cdot)$ reshapes the feature map back to $\mathcal{R}^{W \times H \times \frac{C}{8}}$ and then performs 1×1 convolution. Because the attended illumination

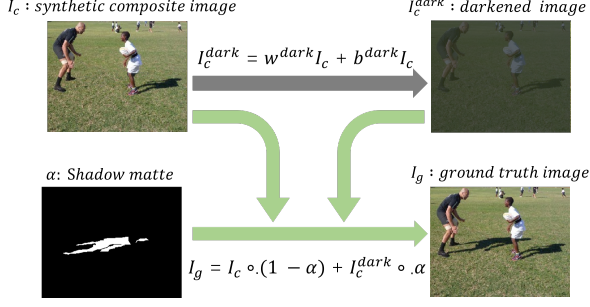


Figure 5. Shadow generation via image composition. The ground-truth target image \mathbf{I}_g with foreground shadow can be expressed as the combination of synthetic composite image \mathbf{I}_c and darkened image \mathbf{I}_c^{dark} with shadow matte α .

information should be combined with the foreground information to generate foreground shadow mask, we concatenate \mathbf{X}'_b and \mathbf{X}_f as \mathbf{X}_{NAI} , which is fed into the decoder D_S to produce foreground shadow mask $\tilde{\mathbf{M}}_{fs}$:

$$\tilde{\mathbf{M}}_{fs} = D_S(\mathbf{X}_{NAI}), \quad (3)$$

which is enforced to be close to the ground-truth foreground shadow mask \mathbf{M}_{fs} by

$$\mathcal{L}_S = \|\mathbf{M}_{fs} - \tilde{\mathbf{M}}_{fs}\|_2^2. \quad (4)$$

4.2. Shadow Area Filling

We design our shadow filling stage based on the illumination model used in [28, 17]. According to [28, 17], the value of a shadow-free pixel $I^{lit}(k, i)$ can be linearly transformed from its shadowed value $I^{dark}(k, i)$:

$$I^{lit}(k, i) = w^{lit}(k) I^{dark}(k, i) + b^{lit}(k), \quad (5)$$

in which $I(k, i)$ represents the value of the pixel i in color channel k ($k \in R, G, B$ color channel). $w^{lit}(k)$ and $b^{lit}(k)$ are constant across all pixels in the umbra area of the shadow. Inversely, the value of a shadowed pixel $I^{dark}(k, i)$ can be linearly transformed from its shadow-free value $I^{lit}(k, i)$:

$$I^{dark}(k, i) = w^{dark}(k) I^{lit}(k, i) + b^{dark}(k). \quad (6)$$

To accurately locate the foreground shadow area, we tend to learn a shadow matte α . The value of α is 0 in the non-shadow area, 1 in the umbra of shadow area, and varying gradually in the penumbra of shadow area. Then, the target image with foreground shadow can be obtained using the following image composition system (see Figure 5):

$$\mathbf{I}_g = \mathbf{I}_c \circ (1 - \alpha) + \mathbf{I}_c^{dark} \circ \alpha, \quad (7)$$

$$\mathbf{I}_c^{dark}(k) = w^{dark}(k) \mathbf{I}_c(k) + b^{dark}(k), \quad (8)$$

in which \circ means element-wise multiplication, $\mathbf{I}(k)$ represents image \mathbf{I} in color channel k , $\mathbf{I}_c^{dark}(k)$ is the darkened version of $\mathbf{I}_c(k)$ through Eqn. 8. $\mathbf{w}^{dark} = [w^{dark}(R), w^{dark}(G), w^{dark}(B)]$ and similarly defined \mathbf{b}^{dark} are referred to as shadow parameters. Given paired images $\{\mathbf{I}_c, \mathbf{I}_g\}$, the ground-truth shadow parameter $\{\mathbf{w}^{dark}, \mathbf{b}^{dark}\}$ for the foreground shadow can be easily calculated by using linear regression. Specifically, we need to calculate the optimal regression coefficients $\{\mathbf{w}^{dark}, \mathbf{b}^{dark}\}$ which regress pixel values $\mathbf{I}_c(k, i)$ to $\mathbf{I}_g(k, i)$ in the foreground shadow area. The ground-truth shadow parameters of training image pairs can be precomputed before training, but the ground-truth shadow parameters of test image pairs are unavailable in the testing stage. Thus, we learn a shadow parameter predictor E_P to estimate $\{\tilde{\mathbf{w}}^{dark}, \tilde{\mathbf{b}}^{dark}\}$.

Our E_P is implemented as an encoder, which takes the concatenation of composite image \mathbf{I}_c and predicted shadow mask $\tilde{\mathbf{M}}_{fs}$ as input to predict the shadow parameters $\{\tilde{\mathbf{w}}^{dark}, \tilde{\mathbf{b}}^{dark}\}$:

$$\{\tilde{\mathbf{w}}^{dark}, \tilde{\mathbf{b}}^{dark}\} = E_P(\mathbf{I}_c, \tilde{\mathbf{M}}_{fs}). \quad (9)$$

$\{\tilde{\mathbf{w}}^{dark}, \tilde{\mathbf{b}}^{dark}\}$ are supervised with ground-truth shadow parameters $\{\mathbf{w}^{dark}, \mathbf{b}^{dark}\}$ by regression loss:

$$\mathcal{L}_P = \|\mathbf{w}^{dark} - \tilde{\mathbf{w}}^{dark}\|_2^2 + \|\mathbf{b}^{dark} - \tilde{\mathbf{b}}^{dark}\|_2^2. \quad (10)$$

After estimating $\{\tilde{\mathbf{w}}^{dark}, \tilde{\mathbf{b}}^{dark}\}$, we can get the darkened image $\tilde{\mathbf{I}}_c^{dark}(k) = \tilde{w}^{dark}(k) \mathbf{I}_c(k) + \tilde{b}^{dark}(k)$ via Eqn. 8. Then, to obtain the final target image, we need to learn a shadow matte $\tilde{\alpha}$ for image composition as in Eqn. 7. Our shadow matte generator G_M is based on U-Net [27] with encoder E_M and decoder D_M . G_M concatenates composite image \mathbf{I}_c , darkened image $\tilde{\mathbf{I}}_c^{dark}$, and predicted shadow mask $\tilde{\mathbf{M}}_{fs}$ as input, producing the shadow matte $\tilde{\alpha}$:

$$\tilde{\alpha} = G_M(\mathbf{I}_c, \tilde{\mathbf{I}}_c^{dark}, \tilde{\mathbf{M}}_{fs}). \quad (11)$$

Finally, based on $\tilde{\mathbf{I}}_c^{dark}$, \mathbf{I}_c , and $\tilde{\alpha}$, the target image with foreground shadow can be composed by

$$\tilde{\mathbf{I}}_g = \mathbf{I}_c \circ (1 - \tilde{\alpha}) + \tilde{\mathbf{I}}_c^{dark} \circ \tilde{\alpha}. \quad (12)$$

The generated target image is supervised by the ground-truth target image with a reconstruction loss:

$$\mathcal{L}_I = \|\mathbf{I}_g - \tilde{\mathbf{I}}_g\|_2^2. \quad (13)$$

4.3. Conditional Discriminator

To ensure that the generated shadow mask $\tilde{\mathbf{M}}_{fs}$ and the generated target image $\tilde{\mathbf{I}}_g$ are close to real shadow mask \mathbf{M}_{fs} and real target image \mathbf{I}_g respectively, we design a conditional discriminator D to bridge the gap between the generated triplet $\{\tilde{\mathbf{M}}_{fs}, \tilde{\mathbf{I}}_g, \mathbf{M}_{fs}\}$ and the real

triplet $\{\mathbf{M}_{fs}, \mathbf{I}_g, \mathbf{M}_{fo}\}$. The architecture of our conditional discriminator is similar to Patch-GAN [14], which takes the concatenation of triplet $\{\mathbf{M}_{fs}, \mathbf{I}_g, \mathbf{M}_{fo}\}$ (*resp.*, $\{\tilde{\mathbf{M}}_{fs}, \tilde{\mathbf{I}}_g, \mathbf{M}_{fo}\}$) as input. We adopt the hinge adversarial loss [25] as follows,

$$\begin{aligned}\mathcal{L}_D &= \mathbb{E}_{\tilde{\mathbf{M}}_{fs}, \tilde{\mathbf{I}}_g, \mathbf{M}_{fo}} [\max(0, 1 + D(\tilde{\mathbf{M}}_{fs}, \tilde{\mathbf{I}}_g, \mathbf{M}_{fo}))] + \\ &\quad \mathbb{E}_{\mathbf{M}_{fs}, \mathbf{I}_g, \mathbf{M}_{fo}} [\max(0, 1 - D(\mathbf{M}_{fs}, \mathbf{I}_g, \mathbf{M}_{fo}))], \\ \mathcal{L}_{GD} &= -\mathbb{E}_{\tilde{\mathbf{M}}_{fs}, \tilde{\mathbf{I}}_g, \mathbf{M}_{fo}} [D(\tilde{\mathbf{M}}_{fs}, \tilde{\mathbf{I}}_g, \mathbf{M}_{fo})].\end{aligned}\quad (14)$$

4.4. Optimization

The overall optimization function can be written as

$$\mathcal{L} = \lambda_S \mathcal{L}_S + \lambda_I \mathcal{L}_I + \lambda_P \mathcal{L}_P + \lambda_{GD} \mathcal{L}_{GD} + \mathcal{L}_D, \quad (15)$$

where λ_S , λ_I , λ_P , and λ_{GD} are trade-off parameters.

The parameters of $\{E_S, NAI, D_S, E_P, E_M, D_M\}$ are denoted as θ_G , while the parameters of D are denoted as θ_D . Following adversarial learning framework [11], we use related loss terms to optimize θ_G and θ_D alternately. In detail, θ_D is optimized by minimizing \mathcal{L}_D . Then, θ_G is optimized by minimizing $\lambda_S \mathcal{L}_S + \lambda_I \mathcal{L}_I + \lambda_P \mathcal{L}_P + \lambda_{GD} \mathcal{L}_{GD}$.

5. Experiments

5.1. Datasets and Implementation Details

We conduct experiments on our constructed DESOBA dataset and real composite images. As mentioned in Section 3, our DESOBA has 11,316 training image pairs and 624 test image pairs, in which 624 test image pairs are further divided into 590 BOS test image pairs and 34 BOS-free test image pairs. The experiments on real composite images will be described in Section 5.6. After a few trials, we set $\lambda_S = \lambda_I = 10$, $\lambda_P = 1$, and $\lambda_{GD} = 0.1$ by observing the generated images during training. We implement our model using PyTorch framework. All images in our used datasets are resized to 256×256 for training and testing. We use adam optimizer with the learning rate initialized as 0.0002 and β set to (0.5, 0.99). The batch size is 1 and our model is trained for 200 epochs.

5.2. Details of Network Architecture

Shadow Mask Generator Our shadow mask generator G_S based on U-Net structure [27] consists of a foreground encoder E_{FS} , a background encoder E_{BS} , a non-local attentional integration layer NAI, and a decoder D_S . Our foreground encoder E_{FS} has 4 downsampling blocks (DBlk), in which each downsampling block consists of 1 convolutional layer with ReLU and batch normalization followed by one downsampling layer. The structure of background encoder E_{BS} is the same as foreground encoder E_{FS} without parameter sharing. Our NAI layer is constructed by four 1×1 convolutional layers, and the structure of NAI

Setting	Training phase	Testing phase
Pix2Pix [14]	11.9M	5.9M
Pix2Pix-Res	11.9M	5.9M
ShadowGAN [46]	21.8M	9.6M
Mask-ShadowGAN [12]	32.5M	27.1M
ARShadowGAN [23]	21.8M	14.6M
SGRNet	18.1M	11.2M

Table 1. Model size comparison among Pix2Pix [14], Pix2Pix-Res, ShadowGAN [46], Mask-ShadowGAN [12], ARShadowGAN [23], and our SGRNet.

layer is shown in Figure 4. Our decoder D_S has 4 upsampling blocks (UBlk), in which each upsampling block is constructed by 1 convolutional layer with ReLU and batch normalization followed by one upsampling layer.

Shadow Parameter Predictor Our shadow parameter predictor E_P is constructed by 4 downsampling blocks (DBlk), 1 Global Average Pooling layer (GAP), and 1 fully-connected (FC) layer, in which each DBlk consists of 1 convolutional layer with ReLU followed by one downsampling layer.

Shadow Matte Generator Our shadow matte generator G_M is also constructed by U-Net [27] with an encoder E_M and a decoder D_M . The structure of E_M (*resp.*, D_M) is the same as E_{FS} (*resp.*, D_S).

Conditional Discriminator To enable the generated shadow mask $\tilde{\mathbf{M}}_{fs}$ and the generated target image $\tilde{\mathbf{I}}_g$ close to real shadow mask \mathbf{M}_{fs} and real target image \mathbf{I}_g , we use conditional discriminator D to distinguish the generated triplet $\{\tilde{\mathbf{M}}_{fs}, \tilde{\mathbf{I}}_g, \mathbf{M}_{fo}\}$ from the real triplet $\{\mathbf{M}_{fs}, \mathbf{I}_g, \mathbf{M}_{fo}\}$. The structure of our D is based on patch-GAN [14], which consists of 4 downsampling blocks (DBlk). Each DBlk has one convolution with valid padding, instance normalization, and LeakyReLU. Then, a convolution produces the last feature map which is activated by sigmoid function.

The Number of Model Parameters We compare the number of model parameters of our SGRNet with Pix2Pix [14], Pix2Pix-Res, ShadowGAN [46], Mask-ShadowGAN [12], and ARShadowGAN [23] in the training stage and testing stage, respectively. In the training stage, The model parameters of generator and discriminator are trainable to complete two-player adversarial learning, while only generator is used to generate target images in the testing stage. In Table 1, we can see that our SGRNet uses fewer model parameters to generate images of better quality compared with Mask-ShadowGAN [12] and ARShadowGAN [23].

5.3. Baselines

Following [23], we select Pix2Pix [14], Pix2Pix-Res, ShadowGAN [46], ARShadowGAN [23], and Mask-

Method	BOS Test Image Pairs					BOS-free Test Image Pairs				
	GR ↓	LR ↓	SSIM ↑	GB ↓	LB ↓	GR ↓	LR ↓	SSIM ↑	GB ↓	LB ↓
Pix2Pix [14]	9.633	82.646	0.926	44.476	88.284	22.292	87.263	0.858	42.639	80.905
Pix2Pix-Res	8.391	83.333	0.971	42.984	85.361	21.756	87.584	0.901	40.843	77.681
ShadowGAN [46]	8.561	85.045	0.985	44.097	87.706	22.381	90.915	0.911	42.056	81.081
Mask-ShadowGAN [12]	10.061	86.505	0.951	47.426	94.141	22.810	89.941	0.893	46.711	88.741
ARShadowGAN [23]	8.613	82.211	0.961	43.631	86.649	22.125	87.312	0.887	41.563	79.105
Ours	6.592	66.223	0.988	26.853	53.431	17.534	62.765	0.923	19.681	37.591

Table 2. Results of quantitative comparison on our DESOBA dataset.

ShadowGAN [12] as baselines. Pix2Pix [14] is a popular image-to-image translation method, which takes composite image as input and outputs target image. Pix2Pix-Res has the same architecture as Pix2Pix except producing a residual image, which is added to the input image to generate the target image. ShadowGAN [46] and ARShadowGAN [23] are two closely related methods, which can be directly applied to our task. Mask-ShadowGAN [12] originally performs both mask-free shadow removal and mask-guided shadow generation. We adapt it to our task by exchanging two generators to perform mask-guided shadow removal and mask-free shadow generation, in which the mask-free shadow generator can be used in our task.

5.4. Performance Metrics

Following [23], we adopt Root Mean Square Error (RMSE), Structural SIMilarity index (SSIM), and Balanced Error Rate (BER) as evaluation metrics. RMSE and SSIM are calculated based on the ground-truth target image and the generated target image. BER is calculated based on the ground-truth binary shadow mask and the generated binary shadow mask, in which the latter is obtained by thresholding the difference between input image and output image with ratio threshold [23]. SSIM, Global RMSE (GR), and Global BER (GB) are calculated over the whole image, while Local RMSE (LR) and Local BER (LB) are calculated over the ground-truth foreground shadow area. Note that LR is not reported in [23] and we add it here for more comprehensive evaluation.

5.5. Evaluation on Our DESOBA Dataset

As mentioned before, we divide DESOBA test set into BOS test set and BOS-free test set, which are evaluated separately. The comparison results on DESOBA dataset are summarized in Table 2. We can observe that our SGRNet achieves the lowest GRMSE, LRMSE, GBER, LBER and the highest SSIM, which demonstrates that our method could generate more realistic and compatible shadows for foreground objects compared with baselines. The difference between the results on BOS test set and BOS-free test set is partially caused by the size of foreground shadow, be-

Method	B-T score ↑
Input Composite	0.612
Pix2Pix [14]	0.587
Pix2Pix-Res	0.708
ShadowGAN [46]	-0.539
Mask-ShadowGAN [12]	-0.232
ARShadowGAN [23]	0.701
SGRNet	2.509

Table 3. B-T scores of different methods on 100 real composite images.

cause BOS-free test image pairs usually have larger foreground shadow than BOS test image pairs as shown in Figure 2. We will provide more in-depth comparison by controlling the foreground shadow size in Section 5.8.

For qualitative comparison, we show some example images generated by our SGRNet and other baselines on BOS and BOS-free test image pairs in Figure 6. We can see that our SGRNet can generally generate foreground shadows with reasonable shapes and shadow directions compatible with the object-shadow pairs in background. In contrast, other baselines produce foreground shadows with implausible shapes, or even fail to produce any shadow.

5.6. Evaluation on Real Composite Images

Since training/test images in DESOBA are synthetic composite images, we further evaluate the effectiveness of our model on real composite images in this section. To obtain real composite images, we select test images from DESOBA as background images, and paste foreground objects also from test images at reasonable locations on the background images. In this way, we create 100 real composite images without foreground shadows for evaluation. The methods in Table 2 are used to generate foreground shadows for composite images.

Because real composite images do not have ground-truth target images, it is impossible to perform quantitative evaluation. Therefore, we conduct user study on the 100 composite images for subjective evaluation. In detail, for each

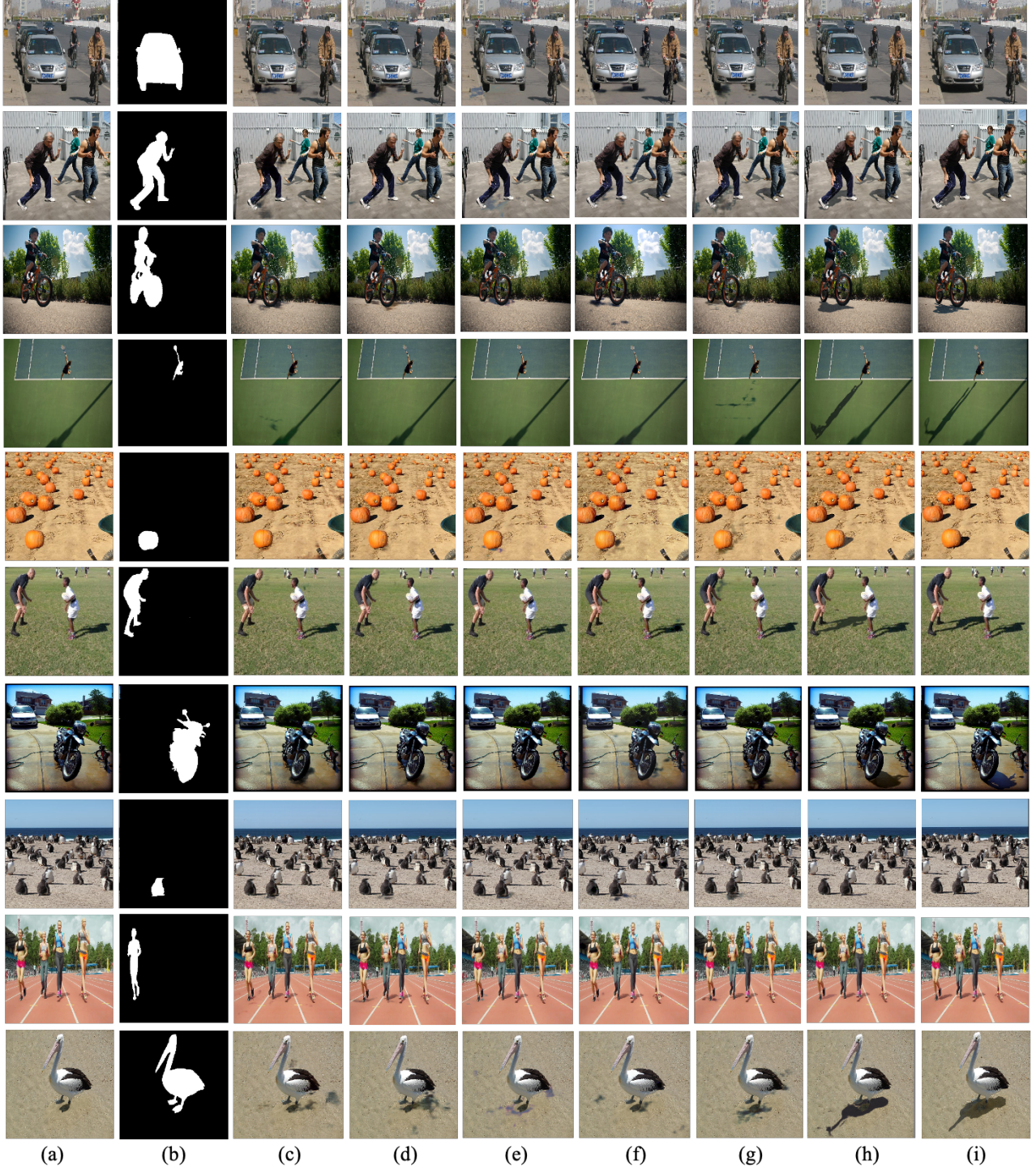


Figure 6. Visualization comparison among different methods on our DESOBA dataset. From left to right are input composite image (a), foreground object mask (b), results of Pix2Pix (c), Pix2Pix-Res (d), ShadowGAN (e), Mask-ShadowGAN (f), ARShadowGAN (g), our SGRNet (h), ground-truth (i). The results on BOS (*resp.*, BOS-free) test image pairs are shown in 1-2 rows (*resp.*, 3-4 rows).

composite image, we can obtain a group of 7 images including the input composite images and the generated im-

ages from 6 methods. We construct pairs within each group of 7 images. Then, we invite 20 human raters to observe a



Figure 7. Visualization comparison with different methods on real composite images. From left to right are background image (a), foreground object mask (b), results of Pix2Pix (c), Pix2Pix-Res (d), ShadowGAN (e), Mask-ShadowGAN (f), ARShadowGAN (g), our SGRNet (h).

pair of images at a time and ask him/her to choose the one with more realistic foreground shadow. Finally, we use the Bradley-Terry model to calculate the global ranking score for each method, which is reported in Table 3. We visualize the comparison results in Figure 7, from which we can see that our SGRNet can generate reasonable foreground shadows for foreground objects, which are compatible with the background object-shadow pairs. Note that the inserted object (*e.g.*, car, airplane) in row 10-11 is from the original background image, which is a special case of image composition.

Because real composite images do not have ground-truth target images, quantitative evaluation cannot be performed. Instead, we conduct user study by asking human raters to select the more realistic image from a pair of images. We employ Bradley-Terry model to calculate the global ranking score for each method and report the B-T score in Table 3. One observation is that the B-T scores of Pix2Pix [14], ShadowGAN [46], and Mask-ShadowGAN [12] are even worse than that of input composite images, which can be explained as follows. Shadows generated by Pix2Pix [14], ShadowGAN [46], and Mask-ShadowGAN [12] often have incomplete and unreasonable shapes incompatible with background information (see Figure 7), making the generated target image even more unrealistic than the input composite image. In contrast, our SGRNet achieves the highest B-T score among all the methods.

5.7. Ablation Studies

We analyze the impact of loss terms and alternative network designs of our SGRNet on BOS test image pairs from DESOBA dataset. Quantitative results are reported in Table 4.

Shadow mask generation stage: To investigate the necessity of background encoder, we remove the background encoder E_{BS} , which is referred to as “w/o E_{BS} ” in Table 4. To verify the effectiveness of non-local attentional integration (NAI) layer, we remove NAI layer and directly concatenate $[X_f, X_b]$, which is referred to as “w/o NAI”. The performance of “w/o NAI” is better than “w/o E_{BS} ”, which shows the advantage of extracting foreground and background information separately. The performance of “w/o NAI” is worse than our full method, which shows the benefit of encouraging thorough information interaction between foreground and background. To study the importance of background object-shadow mask, we set the value of M_{bos} as zero, which is referred to as “w/o M_{bos} ”. The performance is better than “w/o E_{BS} ” and “w/o NAI”, which can be explained as follows. Non-local attention layer can help foreground encoder exploit illumination information from background, even without explicit background object-shadow mask. The comparison between “w/o M_{bos} ” and full method proves that background object-shadow mask

Method	GR ↓	LR ↓	SSIM ↑	GB ↓	LB ↓
w/o E_{BS}	7.907	72.902	0.985	34.716	69.003
w/o NAI	7.187	73.346	0.986	32.043	63.697
w/o M_{bos}	7.016	70.113	0.986	29.995	59.752
w/o Fill	7.293	72.187	0.941	30.912	62.103
w/o \mathcal{L}_P	7.003	73.015	0.986	29.914	59.832
Naive D	7.141	71.182	0.987	31.586	62.847
w/o \mathcal{L}_{GAN}	7.381	70.849	0.986	31.879	63.405
w/o Aug	8.268	74.236	0.984	36.195	71.931
Ours	6.592	66.223	0.988	26.853	53.431

Table 4. Ablation studies of loss terms and alternative network designs on BOS test image pairs from DESOBA dataset.

can indeed provide useful shadow clues as guidance.

Shadow filling stage: To corroborate the superiority of image composition system in section 4, we replace our E_P and $\{E_M, D_M\}$ with a U-Net [27] model which takes \tilde{M}_{fs} and I_c as input to generate the final target image directly, which is referred to as “w/o Fill” in Table 4. The result is worse than full method, which demonstrates the advantage of image composition system. We also remove the supervision for shadow parameters by setting $\mathcal{L}_P = 0$, which is referred to as “w/o \mathcal{L}_P ”. We find that the performance is better than “w/o Fill” but worse than full method, which demonstrates the necessity of supervision from ground-truth shadow parameters.

Adversarial learning: We remove conditional information $\{M_{fo}, M_{fs}\}$ (*resp.*, $\{M_{fo}, \tilde{M}_{fs}\}$), and only feed I_g (*resp.*, \tilde{I}_g) into the discriminator D , which is named as “Naive D” in Table 4. It can be seen that conditional discriminator can enhance the quality of generated images. To further investigate the effect of adversarial learning, we remove the adversarial loss \mathcal{L}_{GD} from Eqn. 15 and report the result as “w/o \mathcal{L}_{GD} ”. The result is worse than “Naive D”, which indicates that adversarial learning can help generate more realistic foreground shadows.

The effect of our augmentation strategy As mentioned in Section 3, to obtain more training image pairs, we choose a subset of foreground objects instead of a single foreground object to create pairs of synthetic composite images and ground-truth target images. In this way, we have in total 11,316 training image pairs. Without this augmentation strategy, we can only have 2999 training image pairs by using a single foreground. We train our SGRNet with 2999 training image pairs and evaluate on BOS test images, which is referred to as “w/o Aug ” in Table 4. It can be seen that this augmentation strategy can improve the performance of our SGRNet by a large margin.

We also visualize some examples produced by different ablated methods in Figure 8. We compare our full-fledged method with ablated versions: “w/o E_{BS} ”, “w/o

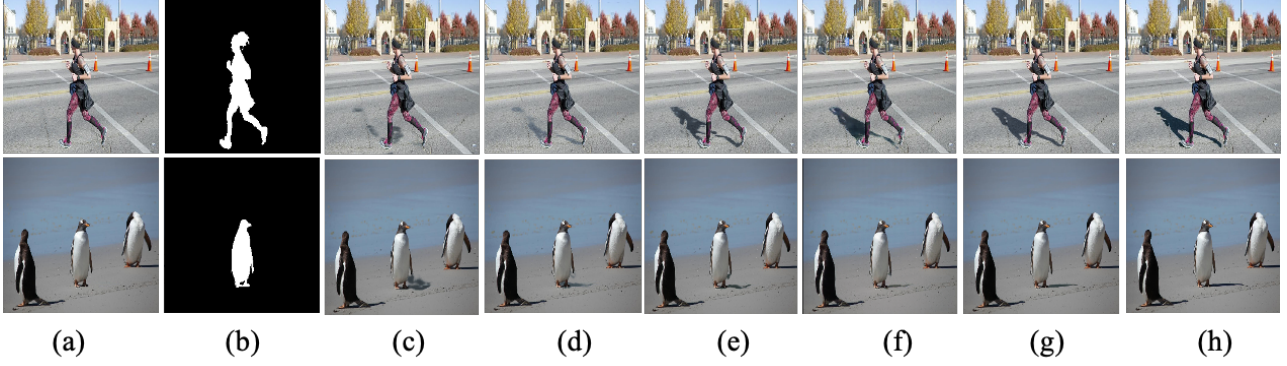


Figure 8. Visualization results of ablated versions of our SGRNet on DESOBA dataset. From left to right are input composite image (a), foreground object mask (b), results of w/o E_{BS} (c), w/o NAI (d), w/o M_{bos} (e), w/o Fill (f), SGRNet (g), ground-truth (h).

Subsets	BOS Test Image Pairs						BOS-free Test Image Pairs					
	NUM	GR ↓	LR ↓	SSIM ↑	GB ↓	LB ↓	NUM	GR ↓	LR ↓	SSIM ↑	GB ↓	LB ↓
$r_{fs} \in (0, 0.02]$	535	5.015	67.761	0.992	28.333	56.492	9	8.663	69.735	0.982	25.721	50.938
$r_{fs} \in (0.02, 0.04]$	32	11.225	49.723	0.964	17.572	34.253	8	15.594	81.791	0.943	25.524	59.783
$r_{fs} \in (0.04, 0.08]$	16	15.143	59.347	0.939	14.474	27.697	8	14.936	54.412	0.927	15.697	30.349
$r_{fs} \in (0.08, 1]$	7	24.506	74.651	0.893	29.407	56.402	9	32.295	76.891	0.807	19.155	35.441
$r_{fs} \in (0, 1]$	590	6.592	66.223	0.988	26.853	53.431	34	17.534	62.765	0.923	19.681	37.591

Table 5. The impact of shadow size on BOS (*resp.*, BOS-free) test images from DESOBA dataset. NUM denotes the number of BOS (*resp.*, BOS-free) test images in each subset. GR (*resp.*, LR) is short for GRMSE (*resp.*, LRMSE). GB (*resp.*, LB) is short for GBER (*resp.*, LBER).

NAI”, “w/o M_{bos} ”, and “w/o Fill”. We visualize some example results produced by different ablated methods in Figure 8. The comparison between these ablated methods and full method proves the advantage of fully exploiting background information and delicate network design based on illumination model.

5.8. The Impact of Shadow Size

To investigate the impact of shadow size as well as the difference between BOS test images and BOS-free test images, we conduct experiments on DESOBA dataset by dividing test images into different subsets according to the foreground shadow ratio r_{fs} (*i.e.*, the area of ground-truth foreground shadow over the area of the whole image). In detail, considering that the foreground shadow ratio is generally smaller than 0.08, we firstly divide BOS and BOS-free test images into 2 subsets: $r_{fs} > 0.08$ and $r_{fs} \leq 0.08$. Then, the subset with $r_{fs} \leq 0.08$ is further divided into 3 subsets: $r_{fs} \in (0, 0.02]$, $r_{fs} \in (0.02, 0.04]$, and $r_{fs} \in (0.04, 0.08]$. In Table 5, we report the numbers of BOS and BOS-free test images in each subset and the results of BOS and BOS-free test images in each subset. It can be seen that GR and SSIM generally become worse when r_{fs} increases, because these two metrics are global evalu-

ation metrics and larger foreground shadow usually lead to worse results. GB is also global metric, but it is a balanced metric and thus less affected by the foreground shadow size.

When comparing the results on BOS-free test images and the results on BOS test images, we do not have consistent conclusions, because the difficulty of generating foreground shadow depends on many factors in a complicated and interlaced way. Although BOS test images have additional shadow clues provided by background object-shadow pairs, BOS-free test images usually have simpler background scenes and a single foreground object located at center, which may make the task easier.

5.9. Visualization of Intermediate Results

To demonstrate the effectiveness of our designed modules including shadow mask generator G_S , shadow parameter predictor E_P , and shadow matte generator G_M , we show some intermediate results. In Figure 9, we show \tilde{M}_{fs} produced by G_S , \tilde{I}_c^{dark} produced after E_P , and $\tilde{\alpha}$ produced by G_M . We can see that our shadow mask generator G_S can infer the shape of foreground shadow. Our shadow parameter predictor E_P can predict reasonable shadow parameters $\{\tilde{w}^{dark}, \tilde{b}^{dark}\}$, which are used to generate darkened images \tilde{I}_c^{dark} . Our shadow matte generator G_M can refine the

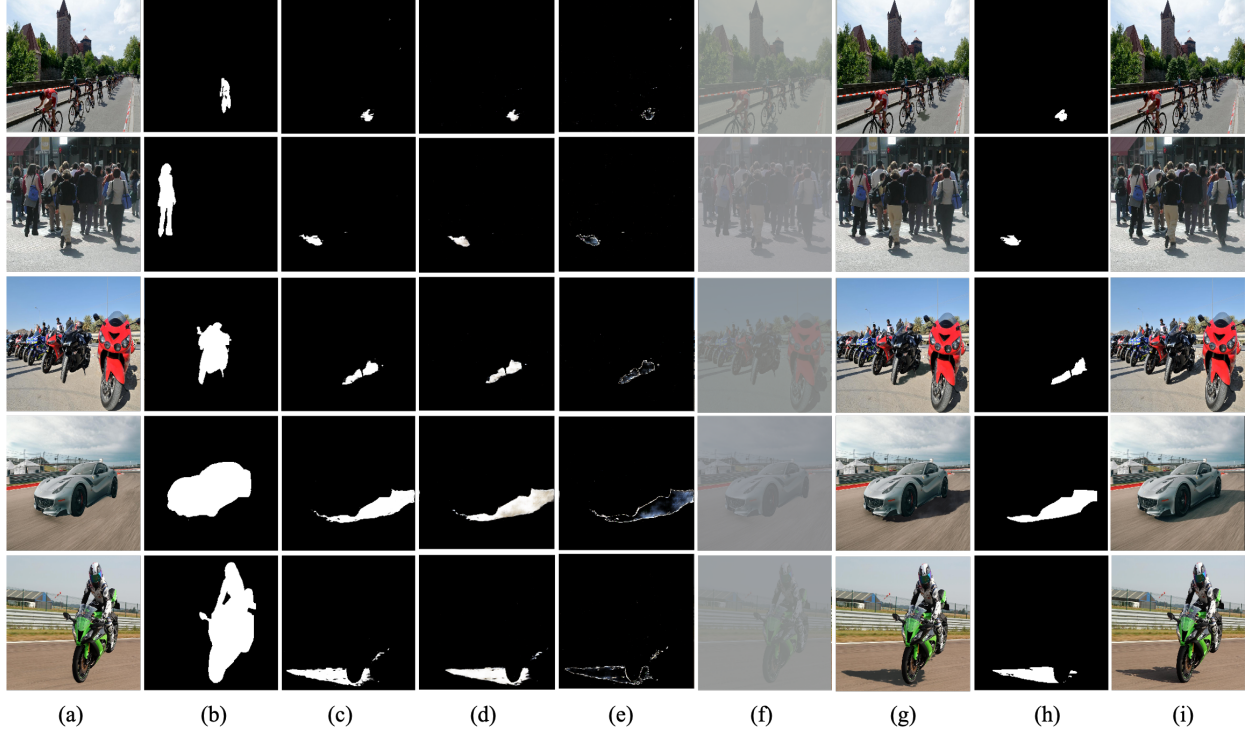


Figure 9. Visualization of intermediate results produced by our SGRNet on DESOBA dataset. From left to right are input composite image I_c (a), foreground object mask M_{fo} (b), generated foreground shadow mask \tilde{M}_{fs} (c), generated shadow matte $\tilde{\alpha}$ (d), the difference between generated foreground shadow mask \tilde{M}_{fs} and the generated shadow matte $\tilde{\alpha}$ (e), generated darkened image \tilde{I}_c^{dark} (f), generated target image \tilde{I}_g (g), ground-truth foreground shadow mask M_{fs} (h), ground-truth target image I_g (i). The results on BOS (*resp.*, BOS-free) test images are shown in row 1-3 (*resp.*, row 4-5).

foreground shadow mask and produce shadow matte of high quality.

5.10. Visualization of Non-local Attentional Integration Layer

We have studied the effectiveness of our Non-local Attentional Integration (NAI) Layer in Section 5.7. To take a deeper look at our NAI layer, we visualize the attention map (A in Eqn. 1) in Figure 10. Recall that for each query pixel in the foreground feature map X_f , we can obtain an $H \times W$ attention map by querying the background feature map X_b . For simplicity, we average the attention maps corresponding to the query pixels in the foreground object area to obtain the integrated attention map in the 3rd column in Figure 10. For better visualization, we impose the integrated attention map on the input composite image, leading to the 4th column in Figure 10. We can see that our designed NAI layer usually pays more attention to the object-shadow areas in the background, probably because background object-shadow areas could provide more clues to infer illumination information.

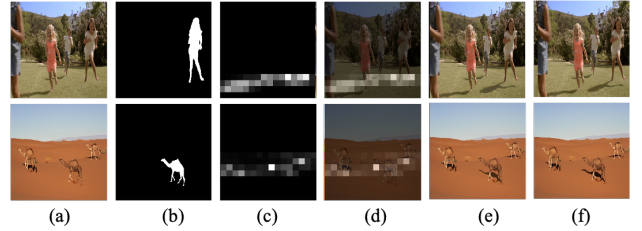


Figure 10. The visualization of learned attention maps from NAI layer. From left to right are input composite image I_c (a), foreground object mask M_{fo} (b), attention map (c), attention map imposed on I_c (d), generated target image \tilde{I}_g (e), ground-truth target image I_g (f).

5.11. Failure Cases

Since our DESOBA dataset is built on the real images, the background scenes and foreground objects could be very complicated. We show some failure cases in Figure 11. In row 1, 2, and 3, our SGRNet can only generate incomplete shadows. In row 4, our SGRNet cannot capture the details of complex foreground object and thus fails to generate

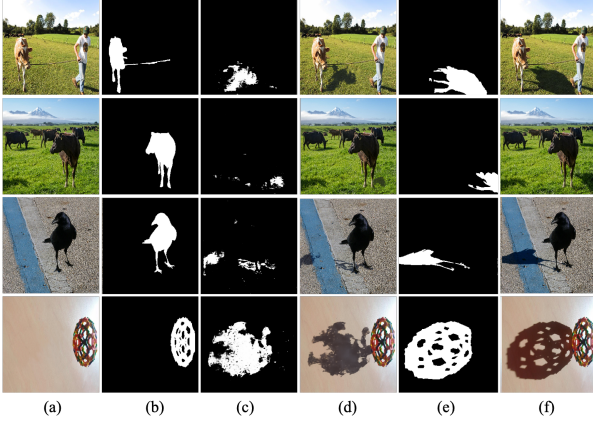


Figure 11. Visualization of failure cases produced by our SGRNet. From left to right are input composite image I_c (a), foreground object mask M_{fo} (b), generated foreground shadow mask \tilde{M}_{fs} (c), generated target image \tilde{I}_g (d), ground-truth foreground shadow mask M_{fs} (e), ground-truth target image I_g (f). The results on BOS (resp., BOS-free) test images are shown in row 1-2 (resp., row 3-4).

compatible foreground shadow.

6. Conclusion

In this work, we have contributed a real-world shadow generation dataset DESOBA. We have also proposed SGRNet, a novel shadow generation method, which can predict shadow mask by inferring illumination information from background and estimate shadow parameters based on illumination model. The effectiveness of our proposed method has been supported by promising results on our constructed dataset and real composite images.

References

- [1] Ibrahim Arief, Simon McCallum, and Jon Yngve Hardeberg. Realtime estimation of illumination direction for augmented reality on mobile devices. In *Color and Imaging Conference*, 2012. 1, 3
- [2] Samaneh Azadi, Deepak Pathak, Sayna Ebrahimi, and Trevor Darrell. Compositional GAN (extended abstract): Learning image-conditional binary composition. In *ICLR 2019 Workshop*, 2019. 1
- [3] Samaneh Azadi, Deepak Pathak, Sayna Ebrahimi, and Trevor Darrell. Compositional gan: Learning image-conditional binary composition. *IJCV*, 128(10):2570–2585, 2020. 1
- [4] Bor-Chun Chen and Andrew Kae. Toward realistic image compositing with adversarial learning. In *CVPR*, 2019. 2
- [5] Dachuan Cheng, Jian Shi, Yanyun Chen, Xiaoming Deng, and Xiaopeng Zhang. Learning scene illumination by pairwise photos from rear and front mobile cameras. *Comput. Graph. Forum*, 37(7):213–221, 2018. 3
- [6] Wenyan Cong, Jianfu Zhang, Li Niu, Liu Liu, Zhixin Ling, Weiyuan Li, and Liqing Zhang. Dovenet: Deep image harmonization via domain verification. In *CVPR*, 2020. 2
- [7] Xiaodong Cun and Chi-Man Pun. Improving the harmony of the composite image by spatial-separated attention module. *TIP*, 2020. 2
- [8] Xiaodong Cun, Chi-Man Pun, and Cheng Shi. Towards ghost-free shadow removal via dual hierarchical aggregation network and shadow matting gan. In *AAAI*, 2020. 2
- [9] Marc-André Gardner, Yannick Hold-Geoffroy, Kalyan Sunkavalli, Christian Gagné, and Jean-Francois Lalonde. Deep parametric indoor lighting estimation. In *ICCV*, 2019. 3
- [10] Marc-André Gardner, Kalyan Sunkavalli, Ersin Yumer, Xiaohui Shen, Emiliano Gambaretto, Christian Gagné, and Jean-François Lalonde. Learning to predict indoor illumination from a single image. *ACM Transactions on Graphics (TOG)*, 36(6):1–14, 2017. 3
- [11] Ishaan Gulrajani, Faruk Ahmed, Martin Arjovsky, Vincent Dumoulin, and Aaron C Courville. Improved training of wasserstein GANs. In *NeurIPS*, 2017. 6
- [12] Xiaowei Hu, Yitong Jiang, Chi-Wing Fu, and Pheng-Ann Heng. Mask-shadowgan: Learning to remove shadows from unpaired data. In *ICCV*, 2019. 2, 3, 6, 7, 10
- [13] Xun Huang, Ming-Yu Liu, Serge Belongie, and Jan Kautz. Multimodal unsupervised image-to-image translation. In *ECCV*, 2018. 2
- [14] Phillip Isola, Jun-Yan Zhu, Tinghui Zhou, and Alexei A Efros. Image-to-image translation with conditional adversarial networks. In *CVPR*, 2017. 2, 6, 7, 10
- [15] Kevin Karsch, Kalyan Sunkavalli, Sunil Hadap, Nathan Carr, Hailin Jin, Rafael Fonte, Michael Sittig, and David Forsyth. Automatic scene inference for 3d object compositing. *ACM Transactions on Graphics (TOG)*, 33(3):1–15, 2014. 2
- [16] Eric Kee, James F. O’Brien, and Hany Samir Farid. Exposing photo manipulation from shading and shadows. *ACM Transactions on Graphics (TOG)*, 2014. 2
- [17] Hieu Le and Dimitris Samaras. Shadow removal via shadow image decomposition. In *ICCV*, 2019. 2, 5
- [18] Hieu Le and Dimitris Samaras. From shadow segmentation to shadow removal. In *ECCV*, 2020. 2
- [19] Bin Liao, Yao Zhu, Chao Liang, Fei Luo, and Chunxia Xiao. Illumination animating and editing in a single picture using scene structure estimation. *Computers & Graphics*, 82:53–64, 2019. 3
- [20] Chen-Hsuan Lin, Ersin Yumer, Oliver Wang, Eli Shechtman, and Simon Lucey. St-gan: Spatial transformer generative adversarial networks for image compositing. In *CVPR*, 2018. 1, 2
- [21] Jianxin Lin, Yingce Xia, Tao Qin, Zhibo Chen, and Tie-Yan Liu. Conditional image-to-image translation. In *CVPR*, 2018. 2
- [22] Bin Liu, Kun Xu, and Ralph R Martin. Static scene illumination estimation from videos with applications. *Journal of Computer Science and Technology*, 32(3):430–442, 2017. 2
- [23] Daquan Liu, Chengjiang Long, Hongpan Zhang, Hanning Yu, Xinzhi Dong, and Chunxia Xiao. Arshadowgan: Shadow

- generative adversarial network for augmented reality in single light scenes. In *CVPR*, 2020. 1, 2, 3, 6, 7
- [24] Takeru Miyato, Toshiki Kataoka, Masanori Koyama, and Yuichi Yoshida. Spectral normalization for generative adversarial networks. In *ICLR*, 2018. 4
- [25] Takeru Miyato and Masanori Koyama. cgans with projection discriminator. In *ICLR*, 2018. 6
- [26] Patrick Pérez, Michel Gangnet, and Andrew Blake. Poisson image editing. In *ACM SIGGRAPH 2003 Papers*, pages 313–318. ACM, 2003. 2
- [27] Olaf Ronneberger, Philipp Fischer, and Thomas Brox. U-net: Convolutional networks for biomedical image segmentation. In *MICCAI*, 2015. 4, 5, 6, 10
- [28] Yael Shor and Dani Lischinski. The shadow meets the mask: Pyramid-based shadow removal. In *Computer Graphics Forum*, volume 27, pages 577–586, 2008. 5
- [29] Yi-Hsuan Tsai, Xiaohui Shen, Zhe Lin, Kalyan Sunkavalli, Xin Lu, and Ming-Hsuan Yang. Deep image harmonization. In *CVPR*, 2017. 2
- [30] Sjoerd van Steenkiste, Karol Kurach, Jürgen Schmidhuber, and Sylvain Gelly. Investigating object compositionality in generative adversarial networks. *Neural Networks*, 130:309–325, 2020. 1
- [31] Ashish Vaswani, Noam Shazeer, Niki Parmar, Jakob Uszkoreit, Llion Jones, Aidan N Gomez, Lukasz Kaiser, and Illia Polosukhin. Attention is all you need. *NeurIPS*, 2017. 4
- [32] Tianyu Wang, Xiaowei Hu, Qiong Wang, Pheng-Ann Heng, and Chi-Wing Fu. Instance shadow detection. In *CVPR*, 2020. 3, 4
- [33] Xiaolong Wang, Ross Girshick, Abhinav Gupta, and Kaiming He. Non-local neural networks. In *CVPR*, 2018. 4
- [34] Shuchen Weng, Wenbo Li, Dawei Li, Hongxia Jin, and Boxin Shi. Misc: Multi-condition injection and spatially-adaptive compositing for conditional person image synthesis. In *CVPR*, 2020. 2
- [35] Huikai Wu, Shuai Zheng, Junge Zhang, and Kaiqi Huang. Gp-gan: Towards realistic high-resolution image blending. In *ACM MM*, 2019. 2
- [36] Su Xue, Aseem Agarwala, Julie Dorsey, and Holly Rushmeier. Understanding and improving the realism of image composites. *ACM Transactions on graphics (TOG)*, 31(4):1–10, 2012. 2
- [37] Fangneng Zhan, Jiaying Huang, and Shijian Lu. Adaptive composition gan towards realistic image synthesis. *arXiv preprint arXiv:1905.04693*, 2019. 2
- [38] Fangneng Zhan, Shijian Lu, Changgong Zhang, Feiying Ma, and Xuansong Xie. Adversarial image composition with auxiliary illumination. In *ACCV*, 2020. 3
- [39] Fangneng Zhan, Shijian Lu, Changgong Zhang, Feiying Ma, and Xuansong Xie. Towards realistic 3d embedding via view alignment. *arXiv preprint arXiv:2007.07066*, 2020. 2
- [40] Fangneng Zhan, Hongyuan Zhu, and Shijian Lu. Spatial fusion gan for image synthesis. In *CVPR*, 2019. 2
- [41] Han Zhang, Ian Goodfellow, Dimitris Metaxas, and Augustus Odena. Self-attention generative adversarial networks. In *ICML*, 2019. 4
- [42] He Zhang, Jianming Zhang, Federico Perazzi, Zhe Lin, and Vishal M Patel. Deep image compositing. In *WACV*, 2021. 2
- [43] Jinsong Zhang, Kalyan Sunkavalli, Yannick Hold-Geoffroy, Sunil Hadap, Jonathan Eisenman, and Jean-François Lalonde. All-weather deep outdoor lighting estimation. In *CVPR*, 2019. 3
- [44] Ling Zhang, Chengjiang Long, Xiaolong Zhang, and Chunxia Xiao. Ris-gan: Explore residual and illumination with generative adversarial networks for shadow removal. In *AAAI*, 2020. 2
- [45] Lingzhi Zhang, Tarmily Wen, and Jianbo Shi. Deep image blending. In *WACV*, 2020. 2
- [46] Shuyang Zhang, Runze Liang, and Miao Wang. Shadowgan: Shadow synthesis for virtual objects with conditional adversarial networks. *Computational Visual Media*, 5(1):105–115, 2019. 1, 2, 3, 4, 6, 7, 10
- [47] Jun-Yan Zhu, Philipp Krahenbuhl, Eli Shechtman, and Alexei A Efros. Learning a discriminative model for the perception of realism in composite images. In *ICCV*, 2015. 2
- [48] Jun-Yan Zhu, Taesung Park, Phillip Isola, and Alexei A Efros. Unpaired image-to-image translation using cycle-consistent adversarial networks. In *ICCV*, 2017. 2